Available online at www.sciencedirect.com
ScienceDirect
Journal of Solid State Chemistry 180 (2007) 2233–2247
JOURNAL OF SOLID STATE CHEMISTRY
www.elsevier.com/locate/jssc

Orthorhombic superstructures within the rare earth strontium-doped cobaltate perovskites: $Ln_{1-x}Sr_xCoO_{3-\delta}$ ($Ln = Y^{3+}$, Dy^{3+}–Yb^{3+}; $0.750 \leqslant x \leqslant 0.875$)

Michael James[a,*], Maxim Avdeev[a], Paris Barnes[b], Liliana Morales[a], Kia Wallwork[c], Ray Withers[d]

[a]Bragg Institute, Building 87, Australian Nuclear Science and Technology Organisation, PMB 1, Menai NSW 2234, Australia
[b]Materials Science Division, MSD 223, Argonne National Laboratory, Argonne, IL 60439, USA
[c]Australian Synchrotron, 800 Blackburn Road, Clayton, Vict. 3168, Australia
[d]Research School of Chemistry, Australian National University, Canberra 0200, ACT, Australia

Received 9 November 2006; received in revised form 29 March 2007; accepted 16 April 2007
Available online 21 May 2007

Abstract

A combination of electron, synchrotron X-ray and neutron powder diffraction reveals a new orthorhombic structure type within the Sr-doped rare earth perovskite cobaltates $Ln_{1-x}Sr_xCoO_{3-\delta}$ ($Ln = Y^{3+}$, Dy^{3+}, Ho^{3+}, Er^{3+}, Tm^{3+} and Yb^{3+}). Electron diffraction shows a *C*-centred cell based on a $2\sqrt{2}a_p \times 4a_p \times 4\sqrt{2}a_p$ superstructure of the basic perovskite unit. Not all of these very weak satellite reflections are evident in the synchrotron X-ray and neutron powder diffraction data and the average structure of each member of this series could only be refined based on *Cmma* symmetry and a $2\sqrt{2}a_p \times 4a_p \times 2\sqrt{2}a_p$ cell. The nature of structural and magnetic ordering in these phases relies on both oxygen vacancy and cation distribution. A small range of solid solution exists where this orthorhombic structure type is observed, centred roughly around the compositions $Ln_{0.2}Sr_{0.8}CoO_{3-\delta}$. In the case of Yb^{3+} the pure orthorhombic phase was only observed for $0.850 \leqslant x \leqslant 0.875$. Tetragonal ($I4/mmm$; $2a_p \times 2a_p \times 4a_p$) superstructures were observed for compositions having higher or lower Sr-doping levels, or for compounds with rare earth ions larger than Dy^{3+}. These orthorhombic phases show mixed valence ($3+/4+$) cobalt oxidation states between $3.2+$ and $3.3+$. DC magnetic susceptibility measurements show an additional magnetic transition for these orthorhombic phases compared to the associated tetragonal compounds with critical temperatures > 330 K.

Keywords: Strontium-doped cobaltate; Neutron diffraction; Perovskite superstructure; Phase diagram; Oxygen vacancy ordering

1. Introduction

Recent years have seen intense interest generated by Sr-doped rare earth cobaltate phases with perovskite structures ($Ln_{1-x}Sr_xCoO_{3-\delta}$) ($Ln$ = lanthanide ion) [1–41]. Studies into their potential application in solid oxide fuel cells [11–13] and as ceramic membranes for high temperature oxygen separation [14–15] have been fuelled by the high electrical and ionic conductivity of these compounds. The magnetic characteristics of these phases have also been the subject of frequent investigations [16–26]. Both structure and properties have been shown to depend critically on the amount and location of oxygen vacancies within these materials, with very small changes in oxygen content driving transitions between metallic ferromagnetic and insulating antiferromagnetic states [24–26].

Strontium-doped rare earth perovskite cobaltates ($Ln_{1-x}Sr_xCoO_{3-\delta}$) show a rich variety of crystal structures depending on the size of the Ln cations, the Sr-doping levels and the amount of oxygen vacancies present. Fig. 1 summarises the phase behaviour of these compounds that have been produced under atmospheric pressures.

*Corresponding author. Fax: +61 2 97 17 3606.
E-mail address: mja@ansto.gov.au (M. James).

0022-4596/$ - see front matter © 2007 Elsevier Inc. All rights reserved.
doi:10.1016/j.jssc.2007.04.029

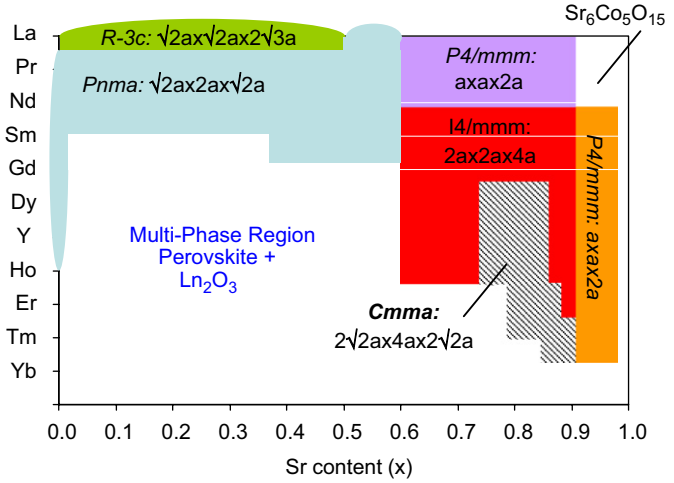

Fig. 1. The perovskite phase diagram for $Ln_{1-x}Sr_xCoO_{3-\delta}$ as a function of rare earth ionic radii and Sr-doping level. The new orthorhombic family is shown by the black and white shaded region.

The largest rare earth elements (La, Pr and Nd) show a wide range of solid solution and a number of different structure types. Lanthanum-based phases show rhombohedral (R-3c) structures for $x \leqslant 0.50$ and a cubic structure for $x = 0.55$ [37]. Compounds containing Pr^{3+} and Nd^{3+} ions on the other hand show orthorhombic (*Pnma*) structures for $x \leqslant 0.5$ [33]. We have recently shown that although all compositions for La^{3+}, Pr^{3+} and Nd^{3+} ($0.7 \leqslant x \leqslant 0.9$) appear metrically cubic by X-ray diffraction they are in fact tetragonal ($P4/mmm$) with an $a_p \times a_p \times 2a_p$ superstructure [7]. Compounds containing intermediate sized rare earth ions (Sm^{3+}, Eu^{3+} and Gd^{3+}) also show (*Pnma*) orthorhombic structures at low doping levels and two-phase regions for $x \leqslant 0.6$ [3,35].

Prior to this study, a number of authors have reported the existence of a tetragonal ($I4/mmm$; $2a_p \times 2a_p \times 4a_p$) perovskite superstructure at room temperature for $0.6 < x \leqslant 0.9$ and for rare earth ions smaller than Nd^{3+} (Fig. 1). We recently described the structural variation of these $Ln_{1-x}Sr_xCoO_{3-\delta}$ tetragonal phases as determined by laboratory powder X-ray diffraction [1,3]; results that were also reported by Istomin et al. [2,4]. The most highly doped members of this perovskite family $Ln_{0.05}Sr_{0.95}CoO_{3-\delta}$ (Y^{3+}, Sm^{3+}–Yb^{3+}) also appear to be metrically cubic according to X-ray diffraction; however, a combination of electron and neutron diffraction reveal a tetragonal ($P4/mmm$ $a_p \times a_p \times 2a_p$) superstructure [5].

Balamurugan and Takayama-Muromachi [25] recently reported the synthesis of an extended series of $Ln_{1-x}Sr_xCoO_3$ phases for $Ln = Y^{3+}$ and Ho^{3+} for $0 \leqslant x \leqslant 1$ under high pressures (6 GPa) and temperatures (1450–1650 °C), and using $KClO_4$ as an oxidizing agent (not shown in Fig. 1). For low Sr^{2+} doping levels ($x = 0$ and 0.2) they indexed their X-ray diffraction data on $\sqrt{2}a_p \times \sqrt{2}a_p \times 2a_p$ orthorhombic cells (although no space group or structures were reported). For high doping levels ($x \geqslant 0.5$ for Y^{3+} and $x \geqslant 0.6$ for Ho^{3+}), including the $SrCoO_3$ end-member, the XRD data were indexed using a simple cubic cell. A two-phase region was reported containing a mixture of the cubic and orthorhombic phases in each case for $x = 0.4$.

Our current study using electron diffraction and high-resolution synchrotron diffraction data reveals that the widely perceived view that there is an extensive phase field based on the tetragonal ($I4/mmm$; $2a_p \times 2a_p \times 4a_p$) superstructure for the smallest rare earth ions is not correct. These techniques show for the first time that a larger orthorhombic cell correctly describes the room temperature symmetry of these materials. In this study we report the structural transitions and phase boundaries of these new orthorhombic phases ($Ln_{1-x}Sr_xCoO_{3-\delta}$; $Ln = Y^{3+}$, Dy^{3+}–Yb^{3+}), which are shown in Fig. 1 by the diagonally shaded region. Detailed structural refinements are given for single-phase, orthorhombic compositions ($Ln_{0.20}Sr_{0.80}CoO_{3-\delta}$; $Ln = Y^{3+}$, Dy^{3+}–Tm^{3+}). In addition, we discuss the magnetostructural correlations present for these compounds.

2. Experimental

2.1. Synthesis

Polycrystalline samples of $Ln_{1-x}Sr_xCoO_{3-\delta}$ ($0.7 \leqslant x \leqslant 0.9$) were prepared from spectroscopic grade powders of $SrCO_3$ (98 + %), $Co(NO_3)_2 \cdot 6H_2O$ (98%) and either Ln_2O_3 (Ln = Y, Nd, Eu, Gd, Dy, Er, Tm and Yb) (≥99.9%), or $Ho(NO_3)_3 \cdot 5H_2O$ (99.9%). The powders were dissolved in dilute nitric acid and an intimate mixture of the metal oxides was formed via the decomposition of a citric acid-ethylene glycol sol–gel at 1000 °C in air. The residues were then ground using an agate mortar and pestle, pelleted and sintered in a tube furnace at 1100 °C under flowing oxygen for up to 3 days with intermediate re-grinding and re-pelleting until no further reaction was evident by powder X-ray diffraction. The samples were slow cooled from 1100 °C to room temperature at a rate of 2 °C min.

2.2. Thermogravimetry

Thermogravimetry of ca. 70 mg of each of the $Ln_{1-x}Sr_xCoO_{3-\delta}$ samples were carried out using a SETARAM TAG24 simultaneous thermogravimetric and differential thermal analyser. The samples were reduced to Ln_2O_3, SrO and Co metal under a mixture of 3.5% hydrogen in nitrogen over a temperature range of 25–950 °C at a heating rate of 5 °C/min.

2.3. Electron diffraction

Electron diffraction (ED) was carried out using a Philips EM 430 transmission electron microscope operating at 300 kV. Samples suitable for TEM work were prepared by the dispersion of finely ground material onto a holey carbon coated copper grid.

Table 1
Refined crystallographic parameters for $Ln_{0.2}Sr_{0.8}CoO_{3-\delta}$ (Ln = Y, Dy, Ho, Er and Tm) from synchrotron X-ray diffraction data

Formula	$Y_{0.2}Sr_{0.8}CoO_{2.69}$	$Dy_{0.2}Sr_{0.8}CoO_{2.71}$	$Ho_{0.2}Sr_{0.8}CoO_{2.75}$	$Er_{0.2}Sr_{0.8}CoO_{2.74}$	$Tm_{0.2}Sr_{0.8}CoO_{2.73}$
CDS-#	417885	471886	417888	417887	417889
Mass	189.850	204.809	206.015	206.625	206.424
Space group	*Cmma*	*Cmma*	*Cmma*	*Cmma*	*Cmma*
Z	32	32	32	32	32
a (Å)	10.8573(1)	10.8497(1)	10.8505(1)	10.8536(1)	10.8431(1)
b (Å)	15.3798(1)	15.3934(1)	15.3705(2)	15.3706(2)	15.3573(1)
c (Å)	10.8188(1)	10.8211(1)	10.8153(1)	10.8107(1)	10.7994(1)
V (Å^3)	1806.56(2)	1807.27(2)	1803.75(3)	1803.51(2)	1798.32(2)
ρ_{calc}	5.584	6.022	6.069	6.088	6.100

2.4. Powder diffraction measurements

Powder diffraction measurements were made on a range of different instruments. Standard X-ray diffraction to check phase purity was carried out with a Panalytical X'Pert Pro diffractometer at ambient temperature using Cu Kα radiation and a flat-plate sample holder. Synchrotron X-ray diffraction data were collected on the ID31 high-resolution powder diffraction beamline ($\lambda = 0.4998$ Å) at the ESRF, Grenoble, France. Powder neutron diffraction data were collected on the HRPD diffractometer ($\lambda = 1.8846$ Å) at the HIFAR facility, Sydney Australia. Structure refinements were carried out by the Rietveld method using the RIETICA program with pseudo-Voigt peak shapes and refined backgrounds. Detailed crystallographic information on these phases have been deposited with the Fachinformationszentrum Karlsruhe, 76344 Eggenstein-Leopoldshafen, Germany, (Fax: +49 7247 808 66; e-mail: crysdata@fiz-karlsruhe.de). Depository numbers for orthorhombic ($x = 0.80$) single-phase samples are listed in Table 1.

2.5. Magnetic measurements

Magnetization data were collected using a quantum design physical properties measurement system (PPMS). The sample was initially zero field cooled (ZFC) to 3 K and DC magnetic susceptibility (χ) measured from 3 to 320 K under an applied field of 100 Oe. High temperature magnetization data were also collected on fresh samples between 300 and 600 K using a Lakeshore Model 7407 vibrating sample magnetometer (VSM) under 100 Oe.

3. Results and discussion

3.1. Oxygen vacancy levels for of $Ln_{0.20}Sr_{0.80}CoO_{3-\delta}$ (Y^{3+}, Gd^{3+}–Tm^{3+})

The overall oxygen content and average cobalt oxidation state for each sample was determined using thermogravimetric analysis. A typical TGA spectrum, scaled to the average cobalt oxidation state (that for $Dy_{0.20}Sr_{0.80}CoO_{3-\delta}$), is shown in Fig. 2. Each of the thermogravimetric profiles show two intermediate weight-loss plateaus between the as-prepared cobalt oxidation state and the fully reduced cobalt metal. The first plateau appears representative of an intermediate Co(III) oxidation state, while the second plateau appears to commence at approximately Co(I). The oxygen contents determined from these TGA data are 2.69(1), 2.72(1), 2.71(1), 2.75(1), 2.74(1) and 2.73(1) for Ln = Y, Gd, Dy, Ho, Er and Tm, respectively, giving rise to average cobalt oxidation states in the as-prepared phases between 3.18 (for $Y_{0.20}Sr_{0.80}CoO_{2.69}$) and 3.30 (for $Ho_{0.20}Sr_{0.80}CoO_{2.75}$).

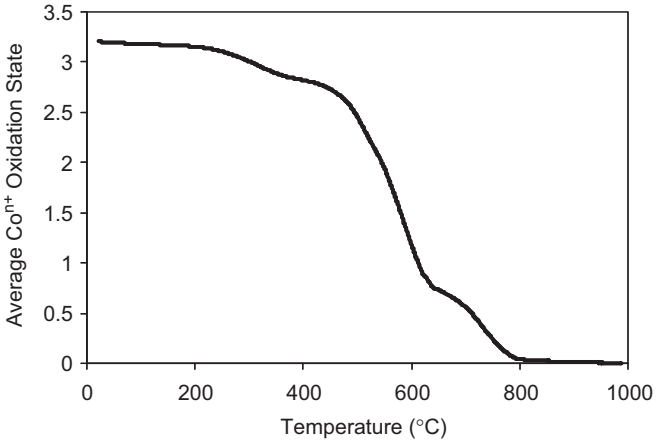

Fig. 2. The TGA mass-loss spectrum of $Dy_{0.20}Sr_{0.80}CoO_{3-\delta}$ reduced under 3.5% H_2 in N_2. The mass-loss (y) axis is re-scaled to reflect the average cobalt oxidation state.

3.2. The new orthorhombic perovskite superstructure of $Ln_{0.20}Sr_{0.80}CoO_{3-\delta}$ (Y^{3+}, Dy^{3+}–Tm^{3+})

High resolution ID31 synchrotron X-ray diffraction data were collected for a range of rare earth ions (Y^{3+}, Nd^{3+}, Eu^{3+}, Gd^{3+}, Dy^{3+}, Ho^{3+}, Er^{3+}, Tm^{3+} and Yb^{3+}) and a range of compositions ($0.70 \leqslant x \leqslant 0.90$). Careful examination of these data collected at 298 K in some cases revealed additional features compared to the ($2a_p \times 2a_p \times 4a_p$) tetragonal cell, such as low angle peaks (e.g. at $d \sim 10.85$ Å) and split reflections. By way of example,

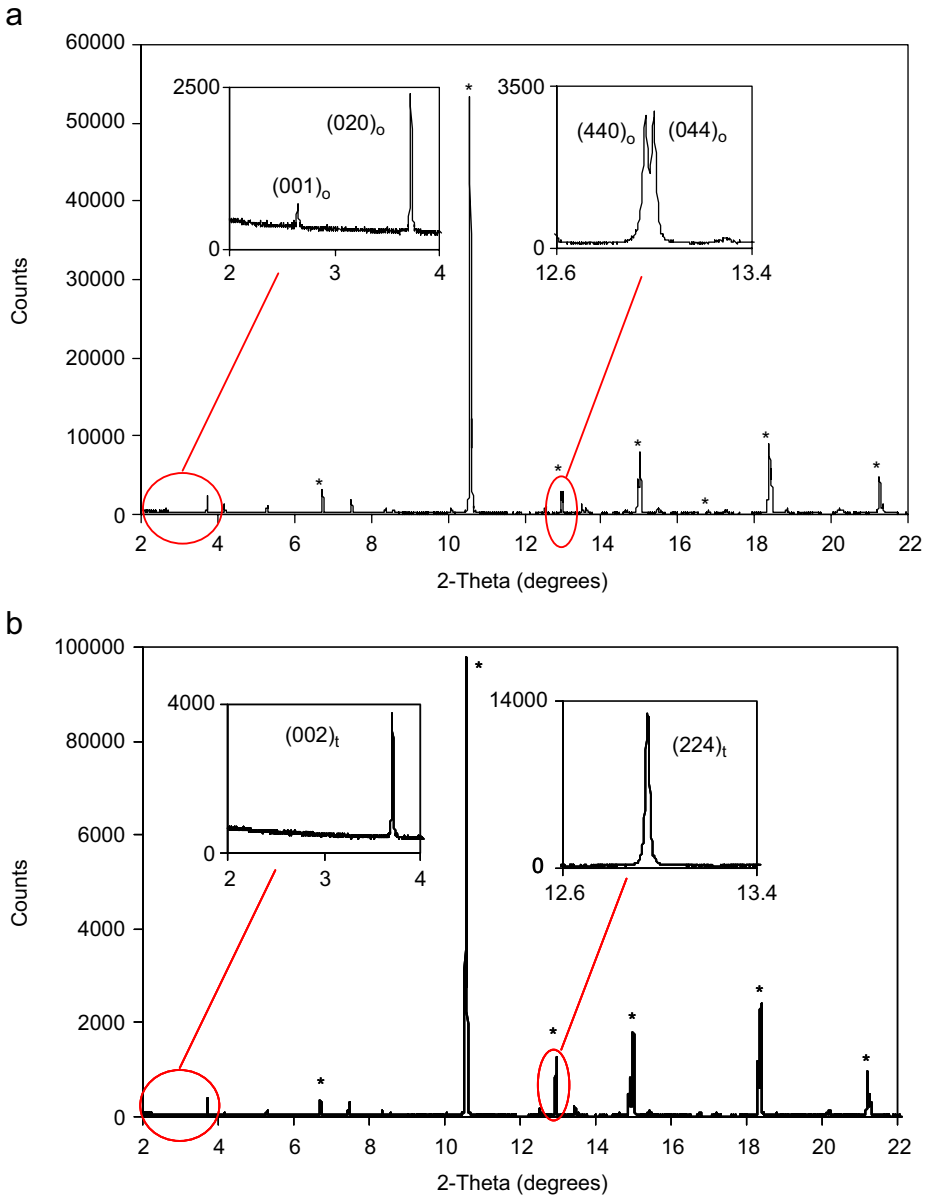

Fig. 3. High-resolution synchrotron X-ray diffraction data for: (a) $Tm_{0.20}Sr_{0.80}CoO_{2.73}$. The left inset shows the very weak (0 0 1) superstructure reflection at d~10.85 Å, while the right inset show the very subtle orthorhombic splitting of the $(1\,1\,1)_p$ parent reflection. (b) The equivalent profile for tetragonal $Gd_{0.20}Sr_{0.80}CoO_{2.72}$. Reflections associated with the perovskite parent structure are indicated by "*".

Fig. 3(a) shows characteristic ID31 X-ray diffraction data for $Tm_{0.20}Sr_{0.80}CoO_{2.73}$, while Fig. 3(b) is for $Gd_{0.20}Sr_{0.80}CoO_{2.72}$. In each case the perovskite parent reflections are indicated by "*". Those additional features shown in Fig. 3(a) were found to be consistent with a $(2\sqrt{2}a_p \times 4a_p \times 2\sqrt{2}a_p)$ orthorhombic cell that was larger than the tetragonal ($I4/mmm$; $2a_p \times 2a_p \times 4a_p$) cell for $Gd_{0.20}Sr_{0.80}CoO_{2.72}$ (Fig. 3(b)) and previously reported for these compositions [3,4]. The ($h\,k\,l$) indices given in the insets of Fig. 3(a) and (b) relate to the orthorhombic and tetragonal cells, respectively. It should also be noted that the b-axis of the orthorhombic cell is equivalent to the c-axis in the tetragonal cell. This arrangement has been chosen so as to describe the orthorhombic cell in the standard *Cmma* crystallographic space group setting (see below). No superstructure reflections characteristic of the orthorhombic cell were observed for compounds containing rare earth elements larger than Dy^{3+}. ID31 data for for $Eu_{0.20}Sr_{0.80}CoO_{2.78}$ could be indexed on the same tetragonal structure as $Gd_{0.20}Sr_{0.80}CoO_{2.72}$, while data for $Nd_{0.20}Sr_{0.80}CoO_{2.80}$ could only be indexed on the simple cubic $Pm\text{-}3\,m$ structure that has been previously reported [7].

Comparison between the synchrotron X-ray diffraction profiles for $Ho_{0.20}Sr_{0.80}CoO_{2.75}$ and $Y_{0.20}Sr_{0.80}CoO_{2.69}$ (Fig. 4) indicates that the observed superstructure is a combination of both cation and oxygen vacancy ordering. Y^{3+} and Sr^{2+} are isoelectronic ($Z = 36$) and thus ordering

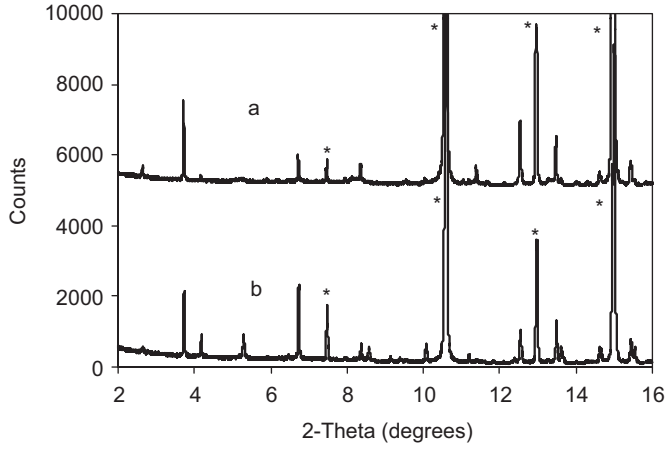

Fig. 4. Synchrotron X-ray diffraction profiles for: (a) $Y_{0.20}Sr_{0.80}CoO_{2.75}$ and (b) $Ho_{0.20}Sr_{0.80}CoO_{2.69}$ indicating both cation and oxygen vacancy ordering contributions to the observed superstructure. Equivalent reflections to the perovskite parent structure are indicated by "*".

between these atoms does not directly lead to superstructure reflections. Superstructure reflections shown in Fig. 4(a) are thus associated with oxygen vacancy ordering. Ho^{3+} on the other hand (with $Z = 64$) provides substantial X-ray contrast with the Sr^{2+} atoms and the additional reflections in Fig. 4(b) are associated with A-site cation ordering.

ED was used to determine the true unit cell and space group symmetry of these phases. Fig. 5 shows (a) a twinned and (b) an untwinned, or single domain, $[0\,1\,0]_p$ (subscript p for the parent perovskite substructure) zone axis ED pattern (EDP) of $Y_{0.20}Sr_{0.80}CoO_{2.69}$. Likewise (c) and (d) show single domain $[1\,0\,1]_p$ and $[-2,1,1]_p$ zone axis EDPs while (e) shows a twinned $[-1,0,1]_p$ zone axis EDP. Careful consideration of these, as well as a range of such EDPs, shows that they can only be consistently indexed with respect to a $2\sqrt{2} \times 4 \times 4\sqrt{2}$, $\mathbf{a} = 2\mathbf{c}_p + 2\mathbf{a}_p$, $\mathbf{b} = 4\mathbf{b}_p$, $\mathbf{c} = -4\mathbf{a}_p + 4\mathbf{c}_p$ ($\mathbf{a}^* = \frac{1}{2}[1\,0\,1]_p^*$, $\mathbf{b}^* = \frac{1}{2}[0\,1\,0]_p^*$, and $\mathbf{c}^* = \frac{1}{8}[-1,0,1]_p^*$) supercell. Indexation without the subscript p in Fig. 5 is with respect to this supercell. (Note that this setting is used so as to be consistent with the smaller *Cmma*, $2\sqrt{2}a_p \times 4a_p \times 2\sqrt{2}a_p$ cell used for the structure refinements reported below). The only systematic extinction conditions observed are $F(hkl) = 0$ unless $h + k = 2J$, J an integer, requiring C-centring and $F(0kl) = 0$ unless $l = 2J$, requiring a c glide perpendicular to **a**. (The apparent breaking of the C-centreing condition in Fig. 5(e) arises because it is a composite pattern formed of an [0 0 1] EDP and a [1 0 0] EDP, as shown on its own in Fig. 5(c). The implied condition for the former [0 0 1] orientation is $F(hk0) = 0$ unless $h + k = 2J$, as required by the C-centreing). The resultant space group symmetry is thus *Cc*- but most probably $Ccm2_1$. Comparison with equivalent EDPs for tetragonal $Ln_{0.1}Sr_{0.9}CoO_{3-\delta}$ phases [3] clearly shows the additional structural modulations that generate the larger orthorhombic cell.

The compound $Tm_{0.20}Sr_{0.80}CoO_{2.73}$ is isomorphous to the Y compound as is apparent from the EDPs shown in Fig. 6. Note that the $\mathbf{G}_p \pm \frac{1}{8}[-1,0,1]_p^*$ and $\mathbf{G}_p \pm \frac{3}{8}[-1,0,1]_p^*$) satellite reflections (*i.e.* the *hkl*, *l* odd, reflections), while always clearly present, are in general significantly weaker than the other satellite reflections. This is most apparent in the $[1\,1\,1]_p$ or $[2\,1\,0]$ zone axis micro-diffraction pattern shown in Fig. 6(c). The weakness of these satellite reflections is presumably why they are not seen via either synchrotron or neutron powder diffraction and force the refinements described below to be carried out in a smaller unit cell and with a different space group symmetry than the true structure.

Attempts to index high-resolution ID31 synchrotron X-ray diffraction profiles for $Ln_{0.20}Sr_{0.80}CoO_{3-\delta}$ ($Ln = Y^{3+}$, Dy^{3+}–Tm^{3+}) using the C-centred $2\sqrt{2}a_p \times 4a_p \times 4\sqrt{2}a_p$ orthorhombic cell found by ED were unsuccessful, and only an assignment of the smaller $2\sqrt{2}a_p \times 4a_p \times 2\sqrt{2}a_p$ cell in subgroup *Cmma* was possible.

Note that there must necessarily be a group–subgroup relationship between this *Cmma*, $2\sqrt{2}a_p \times 4a_p \times 2\sqrt{2}a_p$ average structure and the true *Cc*-, $2\sqrt{2}a_p \times 4a_p \times 4\sqrt{2}a_p$ structure. There are four maximal subgroups of a *Cmma* structure compatible with a doubled c-axis, *Cmca*, *Cmma*, *Ccca* and *Ccma*. The presence of a c glide perpendicular to **a** required by Figs. 5(c) and 6(a), however, rule out all but the latter *Ccma*. Furthermore, the presence of reflections such as 110 in Fig. 5(e), rules out the presence of an a glide perpendicular to **c**. This requires a further lowering of space group symmetry from *Ccma* down to $Ccm2_1$. A resultant space group symmetry of $Ccm2_1$, however, is entirely compatible with all the ED evidence presented above. Knowledge of this space group symmetry constrains the possible structural origin of the $\mathbf{q} = 1/2\mathbf{c}^*$ modulation of the *Cmma* average structure required by the ED evidence. We will return to this point after presenting the results of the average structure refinements.

The structure of $Ho_{0.20}Sr_{0.80}CoO_{2.75}$ (at 298 K) was refined using ID31 synchrotron X-ray and HRPD neutron powder diffraction data and the $2\sqrt{2}a_p \times 4a_p \times 2\sqrt{2}a_p$ cell in *Cmma*. The strong contrast afforded between Ho^{3+} and Sr^{2+} by the synchrotron X-rays allow us to investigate A-site cation ordering between Ho and Sr. Similar values of the neutron scattering length for O ($b = 5.803$ fm) and the Ho, Sr and Co cations ($b = 8.01$, 7.02 and 2.49 fm respectively) means that neutrons are a sensitive probe to the location and quantity of oxygen atoms and vacancies. An initial structural model was developed based on the above supercell with the cations and oxygen atoms on their ideal perovskite positions and the oxygen positions fully occupied. Initially, the Ho^{3+} and Sr^{2+} ions were disordered over the four distinct A-sites. Six unique cobalt sites were present and nine oxygen sites were required to generate the full compliment of anion positions.

In the early stages of the refinement, the synchrotron data were used to determine the location and distribution of the different cations within the structure. As the

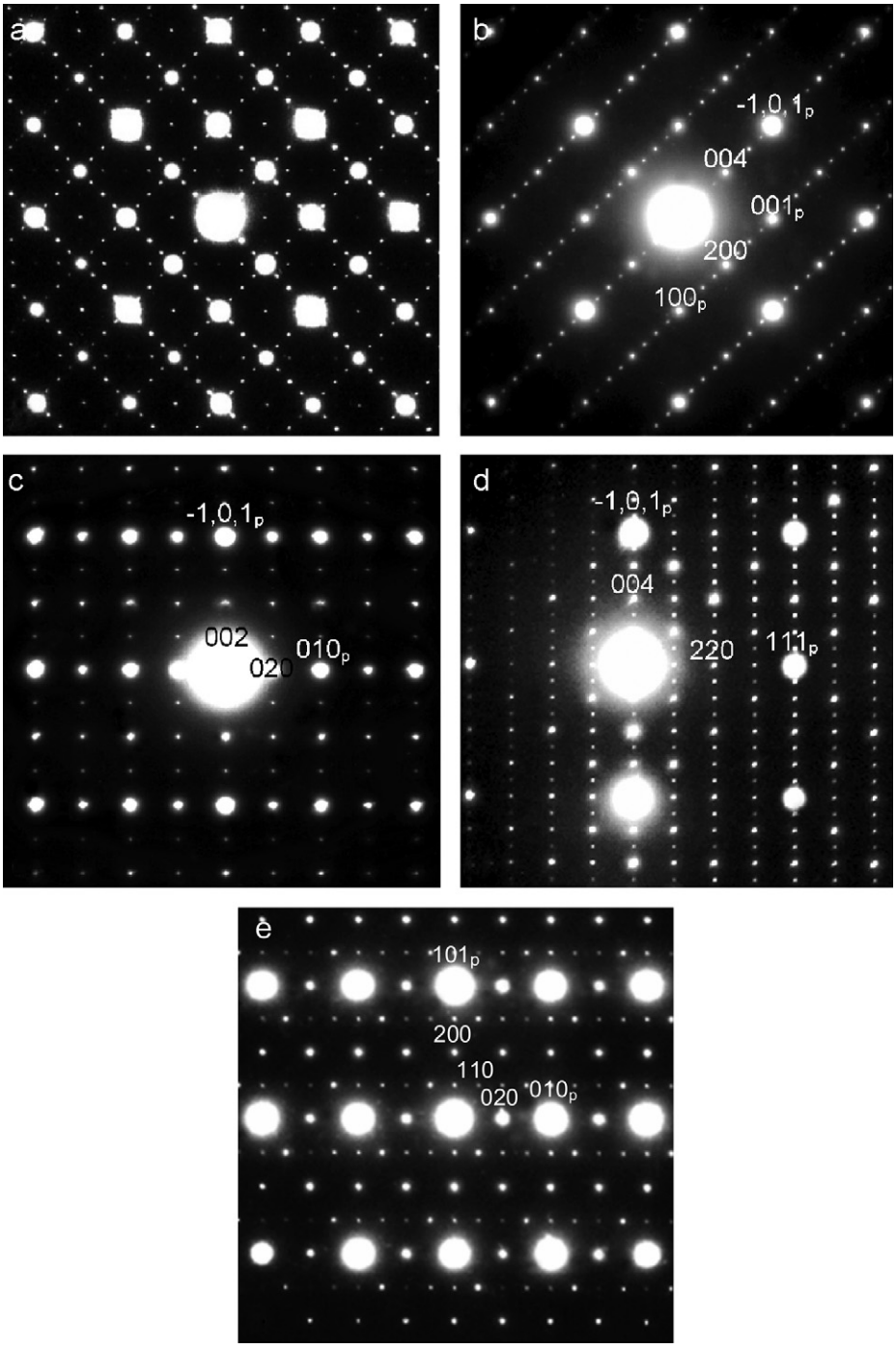

Fig. 5. (a) Twinned and (b) untwinned single domain, $[0\,0\,1]_p$ zone axis electron diffraction pattern (EDP) of $Y_{0.20}Sr_{0.80}CoO_{2.69}$. (c) and (d) show single domain $[0\,1\,1]_p$ and $[-2,1,1]_p$ zone axis EDPs of $Y_{0.20}Sr_{0.80}CoO_{2.69}$ (e) shows a twinned $[-1,0,1]_p$ zone axis EDP.

refinement progressed each of the cations were perturbed from their ideal positions. In all but two cases (Co3 4*c* (0,0,0) and Co4 4*d* (0,0,$\frac{1}{2}$)), the cobalt atoms were found to occupy lower symmetry sites such as the 4 *g* (0,$\frac{1}{4}$,*z*). The A-site cations were each found to leave their ideal perovskite sites and Sr was found to be solely present on three of the four A-sites, with a mixture of 80% Ho and 20% Sr on the fourth 8 *m* (0,*y*,*z*) site (Table 2). As these synchrotron data were found to be relatively insensitive to the location and amount of oxygen present within the structure, the oxygen atoms were initially left in their ideal positions.

This model based on modified cation locations was then used in conjunction with the powder neutron diffraction data to determine the positions of the oxygen atoms. Three types of oxygen sites were generated: 8 *n* (*x*,$\frac{1}{4}$,*z*), 8 *m* (0,*y*,*z*) and the general 16o (*x*,*y*,*z*) position. Of the nine unique oxygen sites in the unit cell, two had abnormally large thermal parameters. Refinement of the occupancy of the

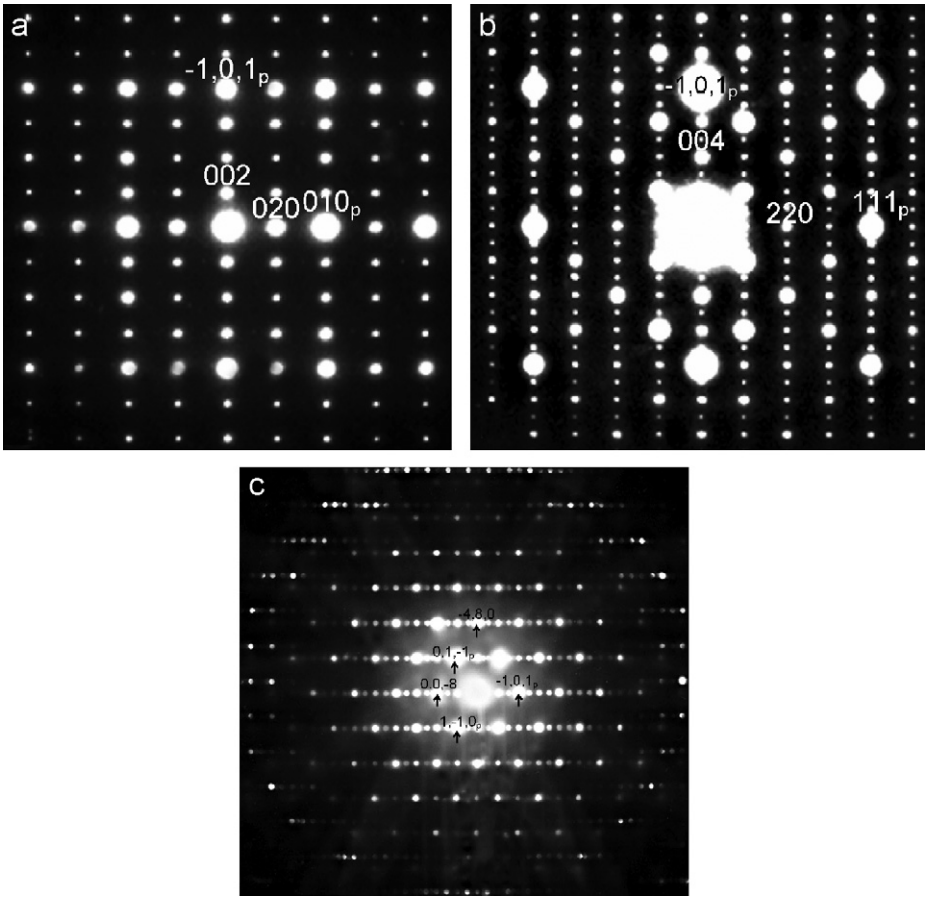

Fig. 6. Electron diffraction patterns for $Tm_{0.20}Sr_{0.80}CoO_{2.73}$ along the: (a) $[0\,1\,1]_p$ and (b) $[-2,1,1]_p$ zone axes. (c) shows the $[1\,1\,1]_p$ or $[1\,2\,0]$ zone axis micro-diffraction pattern.

Table 2
Refined atomic positions and thermal parameters for $Ln_{0.2}Sr_{0.8}CoO_{3-\delta}$ (Ln = Y, Dy, Ho, Er and Tm) from synchrotron X-ray diffraction data

	Site	Y	Dy	Ho	Er	Tm
Co1	$8n$ $(x,\frac{1}{4},z)$					
x	$x\sim\frac{1}{4}$	0.2510(4)	0.2495(4)	0.2531(4)	0.2491(3)	0.2483(3)
z	$y\sim\frac{1}{4}$	0.2551(3)	0.2537(6)	0.2563(6)	0.2510(5)	0.2546(5)
B_{iso}		1.3(1)	1.3(1)	1.4(1)	1.3(1)	1.4(1)
Co2	$4g$ $(0,\frac{1}{4},z)$					
z	$z\sim0$	0.0012(6)	0.0052(7)	0.0051(6)	0.0056(6)	0.0071(7)
B_{iso}		1.3	1.3	1.4	1.3	1.4
Co3	$4c$ (0,0,0)					
B_{iso}		1.3	1.3	1.4	1.3	1.4
Co4	$4d$ $(0,0,\frac{1}{2})$					
B_{iso}		1.3	1.3	1.4	1.3	1.4
Co5	$8l$ $(\frac{1}{4},0,z)$					
z	$z\sim\frac{1}{4}$	0.2498(4)	0.2503(6)	0.2490(6)	0.2546(5)	0.2491(5)
B_{iso}		1.3	1.3	1.4	1.3	1.4
Co6	$4g$ $(0,\frac{1}{4},z)$					
z	$z\sim\frac{1}{2}$	0.5013(6)	0.5066(7)	0.4999(6)	0.5069(5)	0.5053(6)
B_{iso}		1.3	1.3	1.4	1.3	1.4
Sr1	$8j$ $(\frac{1}{4},y,0)$					
y	$y\sim\frac{1}{8}$	0.1182(2)	0.1187(2)	0.1169(2)	0.1188(2)	0.1181(2)
B_{iso}		1.0(1)	1.2(1)	0.8(1)	1.3(1)	1.2(1)

Table 2 (*continued*)

	Site	Y	Dy	Ho	Er	Tm
*Ln*2/Sr2	8 *m* (0,*y*,*z*)					
y	$y\sim\frac{1}{8}$	0.1067(1)	0.1044(1)	0.1050(1)	0.1039(1)	0.1040(1)
z	$z\sim\frac{1}{4}$	0.2538(2)	0.2516(2)	0.2518(2)	0.2539(2)	0.2531(2)
B_{iso}		2.1(1)	2.1(1)	3.0(1)	1.8(1)	1.8(1)
s.o.f		0.80/0.20	0.80/0.20	0.80/0.20	0.80/0.20	0.80/0.20
Sr3	8 *m* (0,*y*,*z*)					
y	$y\sim\frac{1}{8}$	0.1283(1)	0.1273(1)	0.1278(2)	0.1277(1)	0.1277(1)
z	$z\sim\frac{3}{4}$	0.7398(3)	0.7404(3)	0.7370(2)	0.7358(2)	0.7368(3)
B_{iso}		1.5(1)	1.2(1)	1.1(1)	0.8(1)	0.9(1)
Sr4	8*k* ($\frac{1}{4}$,*y*, $\frac{1}{2}$)					
y	$y\sim\frac{1}{8}$	0.1185(2)	0.1185(2)	0.1195(2)	0.1179(2)	0.1187(2)
B_{iso}		1.4(1)	1.0(1)	1.2(1)	1.2(1)	2.0(1)
O1	16*o* (*x*,*y*,*z*)					
x	$x\sim\frac{1}{8}$	0.1207(12)	0.1197(12)	0.1135(13)	0.1211(9)	0.1281(10)
y	$y\sim0$	−0.0086(6)	−0.0092(9)	−0.0124(9)	−0.0114(7)	−0.0148(10)
z	$z\sim\frac{1}{8}$	0.1274(10)	0.1241(12)	0.1295(13)	0.1326(9)	0.1333(9)
B_{iso}		3.0(1)	2.7(1)	3.2(1)	2.6(1)	2.3(1)
O2	16*o* (*x*,*y*,*z*)					
x	$x\sim\frac{1}{8}$	0.1271(11)	0.1285(13)	0.1292(13)	0.1271(9)	0.1143(10)
y	$y\sim0$	−0.0116(6)	−0.0114(9)	−0.0090(10)	−0.0095(7)	−0.0075(9)
z	$z\sim\frac{3}{8}$	0.3824(10)	0.3756(13)	0.3816(13)	0.3818(8)	0.3555(9)
B_{iso}		3.0	2.7	3.2	2.6	2.3
O3	8*n* (x,$\frac{1}{4}$,*z*)					
x	$x\sim\frac{1}{8}$	0.1870(22)	0.1842(22)	0.1877(20)	0.1927(25)	0.1846(24)
z	$z\sim\frac{1}{8}$	0.1068(21)	0.1034(21)	0.0962(19)	0.1144(24)	0.1172(21)
B_{iso}		3.0	2.7	3.2	3.2(2)	2.3
s.o.f		0.24(1)	0.32(1)	0.64(1)	0.14(1)	0.26(1)
O4	8*n* (x,$\frac{1}{4}$,*z*)					
x	$x\sim\frac{3}{8}$	0.3560(17)	0.3474(18)	0.3599(20)	0.3558(14)	0.3764(18)
z	$z\sim\frac{1}{8}$	0.1054(17)	0.1072(17)	0.1005(19)	0.1013(14)	0.1082(16)
B_{iso}		3.0	2.7	3.2	2.6	2.3
O5	8*n* (x,$\frac{1}{4}$,*z*)					
x	$x\sim\frac{1}{8}$	0.0717(22)	0.0736(24)	0.1640(24)	0.0593(21)	0.0609(23)
z	$z\sim\frac{3}{8}$	0.3398(21)	0.3325(21)	0.3891(20)	0.3365(16)	0.3352(18)
B_{iso}		3.0	2.7	3.2	2.6	2.3
s.o.f		0.60(1)	0.58(1)	0.38(1)	0.58(1)	0.56(1)
O6	8*n* (x,$\frac{1}{4}$,*z*)					
x	$x\sim\frac{1}{8}$	0.1285(19)	0.1275(19)	0.1290(20)	0.1298(19)	0.1268(17)
z	$z\sim\frac{5}{8}$	0.6055(21)	0.6237(21)	0.6190(21)	0.6078(16)	0.6111(17)
B_{iso}		3.0	2.7	3.2	2.6	2.3
O7	8 *m* (0,*y*,*z*)					
y	$y\sim\frac{1}{8}$	0.1329(12)	0.1395(16)	0.1355(17)	0.1385(13)	0.1394(15)
z	$z\sim0$	0.0407(12)	0.0345(15)	0.0348(16)	0.0453(11)	0.0304(16)
B_{iso}		3.0	2.7	3.2	2.6	2.3
O8	8 *m* (0,*y*,*z*)					
y	$y\sim\frac{1}{8}$	0.1339(10)	0.1306(18)	0.1266(17)	0.1278(12)	0.1271(14)
z	$z\sim\frac{1}{2}$	0.4797(13)	0.4851(18)	0.4775(17)	0.4886(13)	0.4622(14)
B_{iso}		3.0	2.7	3.2	2.6	2.3
O9	16*o* (*x*,*y*,*z*)					
x	$x\sim\frac{1}{4}$	0.2236(9)	0.2222(8)	0.2250(8)	0.2189(7)	0.2190(8)
y	$y\sim\frac{1}{8}$	0.1316(7)	0.1307(9)	0.1310(9)	0.1351(7)	0.1318(8)
z	$z\sim\frac{1}{4}$	0.2443(9)	0.2386(10)	0.2446(9)	0.2432(8)	0.2413(9)
B_{iso}		3.0	2.7	3.2	2.6	2.3

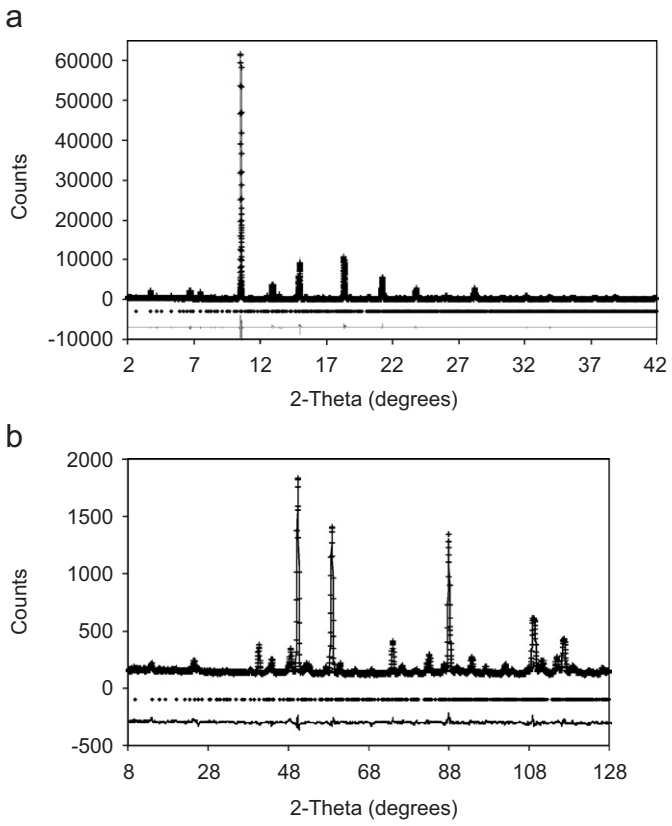

Fig. 7. The observed, calculated and difference profiles for: (a) ID31 synchrotron X-ray and (b) neutron powder diffraction data for $Ho_{0.20}Sr_{0.80}CoO_{2.75}$.

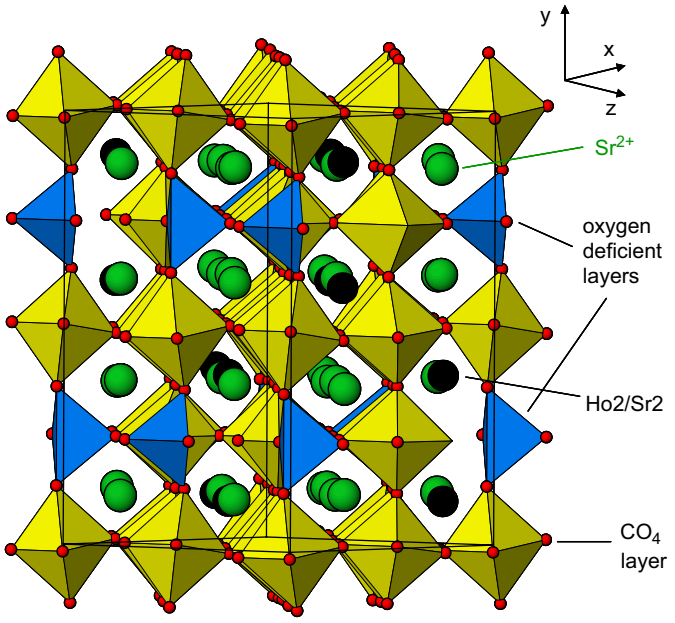

Fig. 8. The refined structure of $Ho_{0.20}Sr_{0.80}CoO_{2.75}$ showing Ho^{3+}/Sr^{2+} cation ordering as well as oxygen vacancy ordering.

oxygen sites showed ordered oxygen vacancies at these two locations (O3 and O5 8*n* $(x,\frac{1}{4},z)$ sites), leading to two oxygen-deficient layers within the structure. The refined occupancies of these oxygen-deficient sites led to an average oxygen content of the structure of 2.77(1), which is in very good agreement with the value of 2.75(1) determined by TGA. Fig. 7 shows the observed, calculated and difference profiles for the synchrotron and neutron powder diffraction data used in this refinement.

The refined structure of $Ho_{0.20}Sr_{0.80}CoO_{2.75}$ is shown in Fig. 8; while Table 1 lists selected refined crystallographic data for this phase. A full listing of the refined atomic positions and thermal parameters for $Ho_{0.20}Sr_{0.80}CoO_{2.75}$ may be found in Table 2. Table 3 contains a listing of the average metal–oxygen bond lengths for the different sites within this structure.

Examination of Fig. 8 and Table 2 shows that the positions of those oxygen sites containing substantial numbers of vacancies in $Ho_{0.20}Sr_{0.80}CoO_{2.75}$ (i.e. O3 and O5) are shifted significantly from their ideal positions, particularly when compared to other fully occupied sites. Aside from oxygen vacancies at these locations, the Co–O coordination sphere was significantly distorted leaving significantly longer distances than usually observed for other rare earth cobaltate perovskites [1–5], where Co(III)–O bond lengths are <2 Å. The Co2–O3 contact

Table 3
Average metal–oxygen bond lengths for $Ln_{0.2}Sr_{0.8}CoO_{3-\delta}$ (Ln = Y, Dy, Ho, Er and Tm) from synchrotron X-ray diffraction data

	Y	Dy	Ho	Er	Tm
Co1–O	1.915	1.900	1.871	1.908	1.928
Co2–O	2.064	2.012	1.984	2.037	1.983
Co3–O	1.968	1.976	1.956	2.031	2.064
Co4–O	1.948	1.969	1.923	1.914	1.955
Co5–O	1.982	1.970	1.985	1.986	1.920
Co6–O	1.836	1.925	1.987	1.882	1.892
Average	1.952	1.959	1.951	1.960	1.957
Sr1–O	2.644	2.614	2.644	2.646	2.647
*Ln*2/Sr2–O	2.674	2.677	2.867	2.661	2.609
Sr3–O	2.832	2.826	2.816	2.843	2.797
Sr4–O	2.780	2.819	2.656	2.799	2.880
Average	2.733	2.734	2.746	2.737	2.733

distance in $Ho_{0.20}Sr_{0.80}CoO_{2.75}$ is 2.262 Å, while the Co6–O5 distance is 2.145 Å; which are substantially longer than axial Co–O bonds observed for tetragonally distorted K_2NiF_4-based rare earth cobaltates such as $La_{1.25}Sr_{0.75}CoO_4$ (2.075 Å) [42]. Fig. 8 shows that these oxygen deficient positions are confined only to the $y=\frac{1}{4}$ and $\frac{3}{4}$ layers of the structure, but interestingly the O6 oxygen also located in these layers did not show any evidence of vacancies. In contrast, the Ho2/Sr2 cation ordering is present in each of the A-site layers along the *y*-axis.

The room temperature structures of the other $Ln_{0.20}Sr_{0.80}CoO_{3-\delta}$ phases ($Ln = Y^{3+}$, Dy^{3+}, Er^{3+} and Tm^{3+}) were also determined using ID31 synchrotron data.

Although data was collected for the "$Yb_{0.20}Sr_{0.80}CoO_{3-\delta}$" composition, this sample was shown to contain impurities (such as Yb_2O_3) and a structure was not refined for this multi-phase system. Although the main phase is perovskite in nature and shows clear indicators of being orthorhombic, given the presence of Yb_2O_3 the A-site cation ratio (Yb^{3+}:Sr^{2+}) would no longer be 0.20:0.80.

Of the lanthanide atoms in this series, Ho had the lowest neutron adsorption cross-section (64.7 barn), making it suitable for a combined Rietveld refinement based on synchrotron X-ray and neutron powder diffraction data. By way of contrast Dy has a substantially larger adsorption cross-section (994 barn) (even larger than atoms such as boron found in neutron shielding) making $Dy_{0.20}Sr_{0.80}CoO_{2.71}$ unsuitable for study by thermal neutrons. Starting models for the refinements of compounds containing Y^{3+}, Dy^{3+}, Er^{3+} and Tm^{3+} based on synchrotron X-ray data were taken from the structure of $Ho_{0.20}Sr_{0.80}CoO_{2.75}$.

Each of these phases was found to be isostructural with the holmium analogue, with the same cation and oxygen vacancy distributions. The assignment of the correct symmetry for these $Ln_{0.20}Sr_{0.80}CoO_{3-\delta}$ phases was made possible via the excellent signal-to-noise and the very high resolution afforded by the ID31 synchrotron X-ray powder diffractometer. The orthorhombic distortions determined from these refined structures range between 1.0014 and 1.0032 for b/a and between 1.0049 and 1.0059 for b/c.

Although the positions of a number of the cobalt atoms for these $Ln_{0.20}Sr_{0.80}CoO_{3-\delta}$ compounds could be considered to be located at their "ideal" sites to within their estimated standard deviations (Table 2), the orthorhombic *Cmma* symmetry allows them to occupy more general sites. When one compares the refined cobalt atom locations between different compounds it becomes apparent that the assignment of these general sites is correct. For example, the z position at the $4g$ $(0,\frac{1}{4},z)$ Co6 site for $Ho_{0.20}Sr_{0.80}CoO_{2.75}$ is located at 0.4999(6), while the location for $Tm_{0.20}Sr_{0.80}CoO_{2.73}$ is clearly not on the ideal site at 0.5032(6).

The structures of $Ho_{0.30}Sr_{0.70}CoO_{3-\delta}$ and $Ho_{0.10}Sr_{0.90}CoO_{3-\delta}$ were also refined from ID31 synchrotron X-ray diffraction data and were found to be the same as previously reported [1–4]. The arrangement of atoms in the oxygen-deficient layers are compared for $Ho_{0.20}Sr_{0.80}CoO_{2.75}$ (Fig. 9(a)) and $Ho_{0.30}Sr_{0.70}CoO_{3-\delta}$ (Fig. 9(b)) with the A-site Ho^{3+} and Sr^{2+} cations shown for the adjacent layers. The unit cells drawn for Fig. 9(a) and (b) refer to the orthorhombic (*Cmma*) and tetragonal (*I*4/*mmm*) cells, respectively, with their long ($4a_p$) unit cell axis normal to the page. The tetrahedral CoO_4 polyhedra are shown in blue, while the Ho2/Sr2 atoms are shown in black. The layer for Fig. 9(a) was centred on $y=\frac{3}{4}$, while that for Fig. 9(b) was centred on $z=0$. The A-site cation arrangements for $Ho_{0.20}Sr_{0.80}CoO_{2.75}$ and $Ho_{0.30}Sr_{0.70}CoO_{3-\delta}$ were found to be essentially the same; although the additional Ho^{3+} in the latter compound led to the complete occupation of the Ho2 site and a 10% occupancy of the Ho1/Sr1 site. In $Ho_{0.20}Sr_{0.80}CoO_{2.75}$ the equivalent site was fully occupied by Sr^{2+}. Fig. 9(a) shows that the oxygen-deficient layer consists of a mixture of tetrahedrally and octahedrally coordinated cobalt ions with the CoO_4 tetrahedra are aligned along the crystallographic x-axis. As previously noted the O3 and O5 sites were partially occupied along with an associated distortion of the octahedra. No complete CoO_6 octahedra were found in $Ho_{0.30}Sr_{0.70}CoO_{3-\delta}$, where the coordination could be described by tetrahedra aligned in both directions in the basal plane and a partially occupied O4 atom.

Returning to the question of what the additional $\mathbf{q}=\frac{1}{2}\mathbf{c}^*$ modulation of the refined *Cmma* average structure could be due to, consider the oxygen-deficient layer for $Ho_{0.20}Sr_{0.80}CoO_{2.75}$ at $y=\frac{3}{4}$ in projection along **b** (Fig. 9(a)). Two parent unit cells along the c direction are shown. An $1\times1\times2$ resultant supercell space group symmetry of $Ccm2_1$ does not allow the supercell to be associated with additional ordering of the Ho and Sr ions occupying the Ho2/Sr2 site. It does, however, allow additional oxygen ordering on both the O3 and O5 sites but only in a very specific manner.

$Ccm2_1$ only allows the occupancies of sites related by the mirror plane perpendicular to **a** in the *Cmma* average structure, i.e. $O3_1/O3_2$, $O5_1/O5_2$, etc to vary in the opposite sense (if the occupancy of $O5_1$ increases towards 1 then simultaneously the occupancy of $O5_2$ must reduce towards zero). The reverse would be the case in the next average structure unit cell along the c direction. Note that the coordination polyhedron surrounding Co6 would thus be reduced to square pyramidal rather than distorted octahedral. The same rules apply for both the $y=\frac{1}{4}$ and $\frac{3}{4}$ layers. As there is no symmetry operation for $Ccm2_1$ linking the two layers, however, the oxygen ordering patterns in each layer needed to be refined independently.

3.3. The orthorhombic phase field

Careful examination of high-resolution synchrotron X-ray diffraction data for a substantial number of synthetic compositions reveals the extent of the orthorhombic phase field for these compounds. The results are summarized by the diagonally shaded area in Fig. 1. No orthorhombic superstructure was observed for any compositions containing Eu^{3+} or Gd^{3+}; while Dy^{3+}, Y^{3+} and Ho^{3+} showed signature peaks for $0.750\leqslant x\leqslant0.850$. Either side of this range of compositions, the *I*4/*mmm* ($2a_p\times2a_p\times4a_p$) superstructure was observed as previously reported [4]. In the case of Tm^{3+} and Er^{3+} single phase orthorhombic samples were observed for $0.775\leqslant x\leqslant0.875$. Compositions with $x<0.775$ were also found to be orthorhombic but contain the impurity Ln_2O_3. $Ln_{0.10}Sr_{0.90}CoO_{3-\delta}$ (Ln = Er and Tm) were found to be phase-pure and tetragonal. Similar behaviour was observed for samples containing Yb^{3+}, however in this case, the two-phase region containing orthorhombic material was

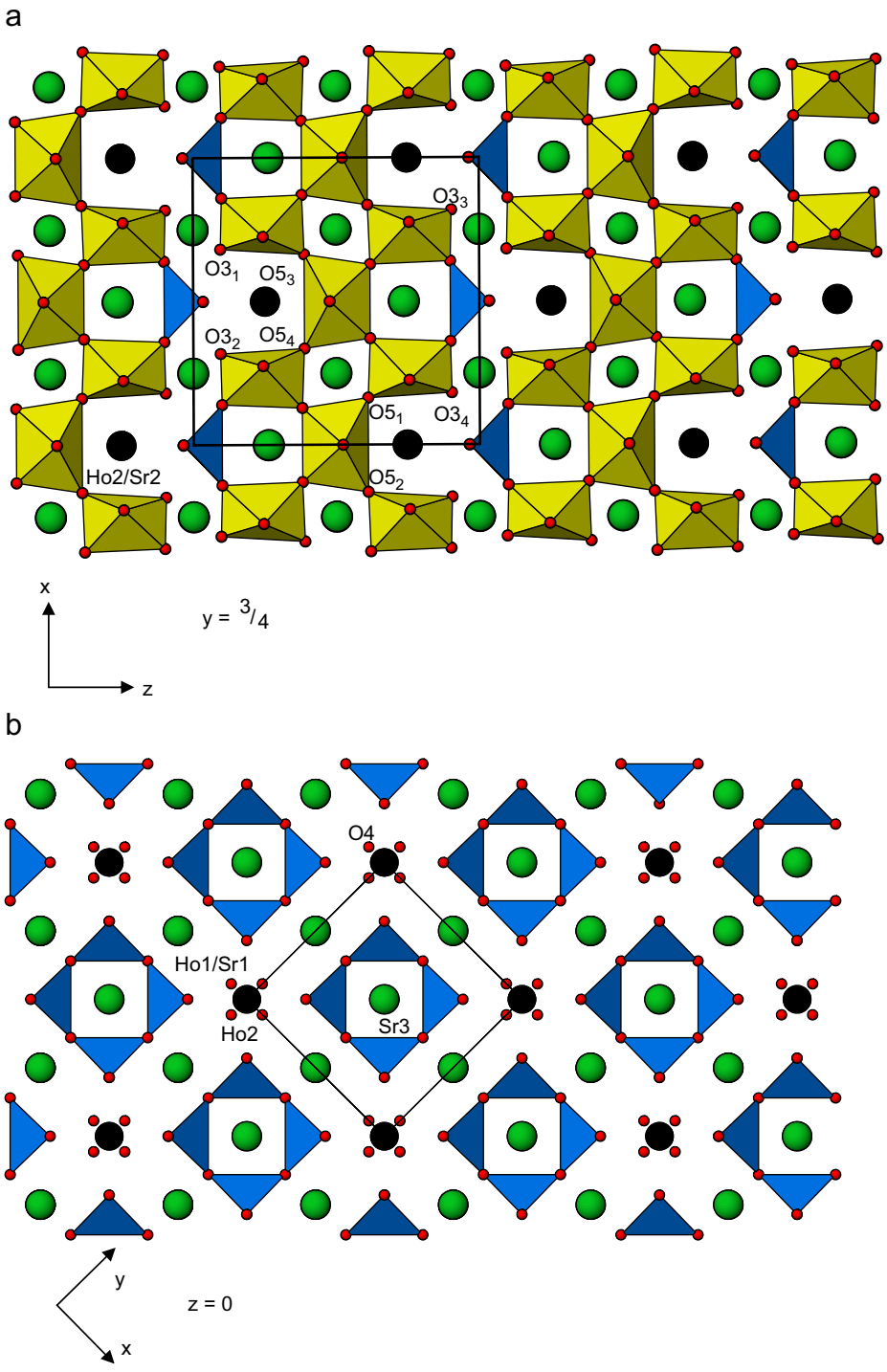

Fig. 9. Local structure within the oxygen-deficient layers of: (a) orthorhombic $Ho_{0.2}Sr_{0.8}CoO_{2.75}$ and (b) tetragonal $Ho_{0.30}Sr_{0.70}CoO_{3-\delta}$.

observed for $x<0.825$ and a pure orthorhombic phase for $0.825\leqslant x\leqslant 0.875$.

The evolution of the lattice parameters across the orthorhombic phase field with x are shown for $Ln = Dy^{3+}$, Ho^{3+}, Tm^{3+} and Yb^{3+} in Figs. 10(a)–(d). So that these structural trends may be more readily observed, all of the unit cell parameters have been reduced to be equivalent to the a parameter of the tetragonal cell (~7.65 Å). Again, it should be noted that the c parameter of the tetragonal cell is the equivalent axis to the b parameter of the orthorhombic cell. Both the Dy^{3+} and Ho^{3+} analogues show splitting of the tetragonal a axis above x ~0.725 which increases across the orthorhombic phase field (Figs. 10(a) and (b)). Above the upper limit (x ~0.85) the additional orthorhombic superstructure peaks and peak splittings disappear, with the superstructure reverting back to the

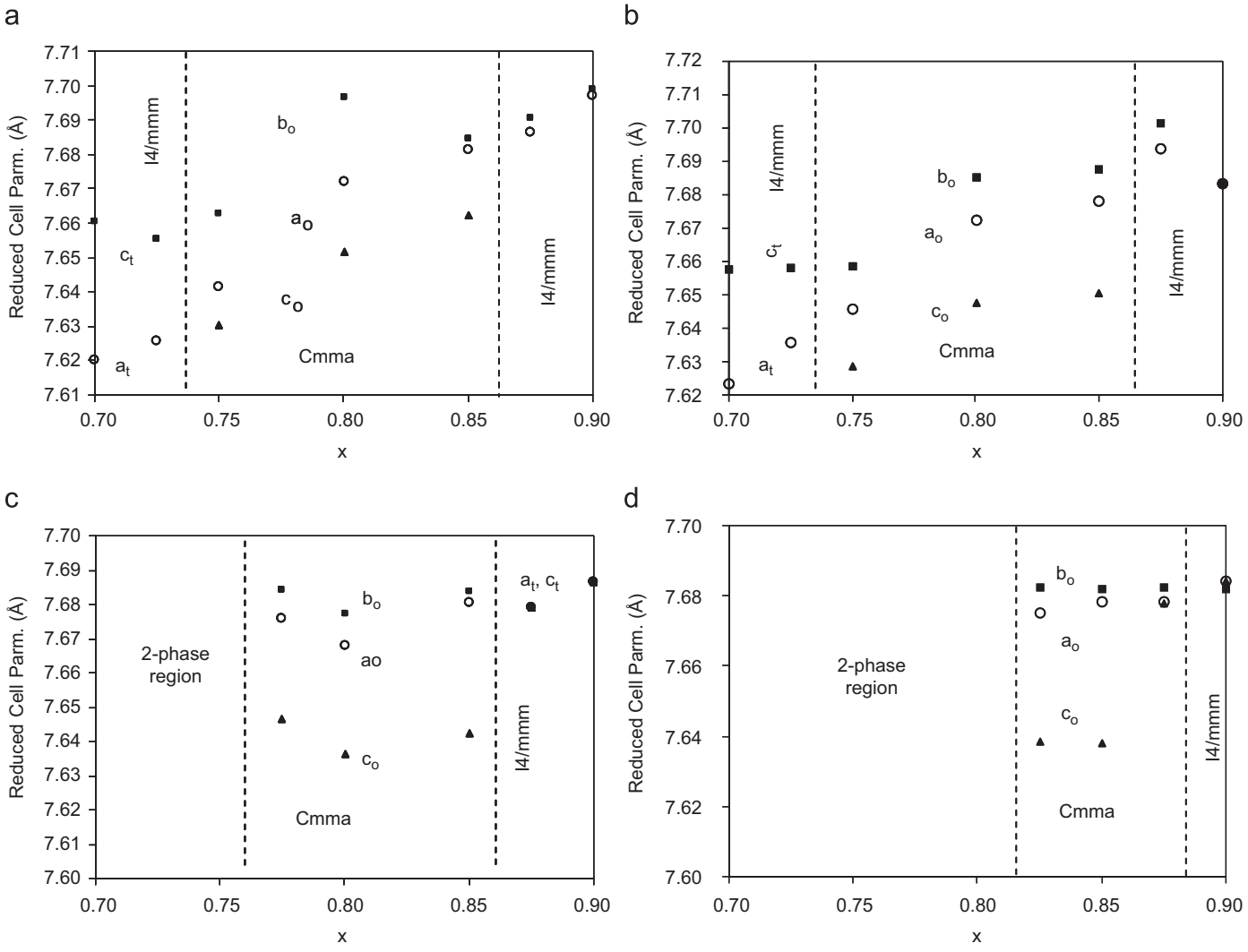

Fig. 10. Evolution of lattice parameters across the orthorhombic phase field with x are shown for $Ln_{0.20}Sr_{0.80}CoO_{3-\delta}$ (Ln = (a) Dy^{3+}, (b) Ho^{3+}, (c) Tm^{3+} and (d) Yb^{3+}).

tetragonal cell. At $x = 0.90$ all three peaks converge to a metrically cubic unit cell, which our previous study using electron and neutron powder diffraction have established retains tetragonal symmetry [4]. The orthorhombic lattice parameters show similar characteristics for Tm^{3+} and Yb^{3+} compounds (Figs. 10(c) and (d)), although careful examination of these synchrotron diffraction data shows that the structure of the major (perovskite) phase remains orthorhombic in the two-phase region.

3.4. Magnetic behaviour of $Ln_{0.20}Sr_{0.80}CoO_{3-\delta}$ (Gd^{3+}–Tm^{3+})

Magnetic DC susceptibility data were collected for each member of the $Ln_{0.20}Sr_{0.80}CoO_{3-\delta}$ ($Ln = Gd^{3+}$–Tm^{3+}) series, as well as for $Ho_{0.30}Sr_{0.70}CoO_{3-\delta}$ and $Ho_{0.10}Sr_{0.90}CoO_{3-\delta}$ between 3 and 600 K. Data for $Gd_{0.20}Sr_{0.80}CoO_{2.72}$ are shown in Fig. 11(a), while equivalent data are shown for $Ho_{1-x}Sr_xCoO_{3-\delta}$ ($x = 0.70$, 0.80 and 0.90) in Fig. 11(b). In each case, a number of magnetic transitions were observed, although the behaviour for (tetragonal) $Gd_{0.20}Sr_{0.80}CoO_{2.72}$ differed significantly from the other (orthorhombic) members of this series. The magnetic susceptibility data for $Ho_{0.20}Sr_{0.80}CoO_{2.75}$ were representative of the other orthorhombic phases ($Ln = Dy^{3+}$, Er^{3+} and Tm^{3+}). Critical temperatures (T_c) for transitions in these compounds are listed in Table 4, along with Curie constants (C_M), effective moments (μ_{eff}) and Weiss parameters (θ) determined from the high temperature (> 400 K) paramagnetic region. Weiss parameters vary from 13.2 K (for $Er_{0.20}Sr_{0.80}CoO_{2.74}$) to 67.3 K (for $Gd_{0.20}Sr_{0.80}CoO_{2.72}$), and in each case the positive values correspond to antiferromagnetic interactions.

From these high temperature paramagnetic susceptibility data one can extract effective moments (μ_{eff}) per mole of compound (Table 4). If one then takes account of the contribution from the 0.2 mol of rare earth ions, the average Co^{n+} moment can be calculated; with values

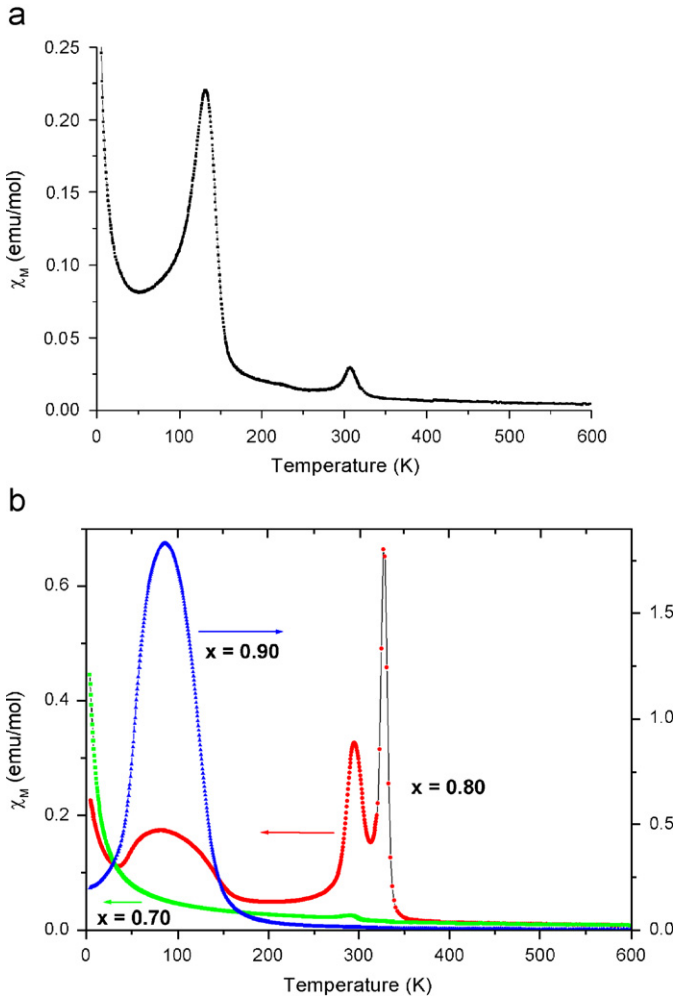

Fig. 11. DC magnetic susceptibility data between 3 and 600 K for: (a) $Gd_{0.20}Sr_{0.80}CoO_{3-\delta}$ and (b) $Ho_{1-x}Sr_xCoO_{3-\delta}$ ($x = 0.70$, 0.80 and 0.90).

Table 4
Magnetic parameters for $Ln_{0.2}Sr_{0.8}CoO_{3-\delta}$ (Ln = Gd, Dy, Ho, Er and Tm) determined from χ_M vs T data, ground state configurations and effective ionic moments (μ_{eff})

Ln	Gd	Dy	Ho	Er	Tm
δ[a]	0.28	0.29	0.25	0.26	0.27
% Co^{4+}	23%	21%	30%	27%	25%
Critical temperatures (K)					
T_{c1}	—	342	333	348	340
T_{c2}	307	283	298	318	307
T_{c3}	131	117	120	–	104
C_M (emu K mol^{-1})	1.90	3.60	2.96	2.38	1.78
θ(K)	67.3	42.8	59.1	13.2	56.8
Observed μ_{eff} (μ_B)	3.90	5.37	4.86	4.36	3.77
No. unpaired *f* electrons	7 ($4f^7$)	5 ($4f^9$)	4 ($4f^{10}$)	3 ($4f^{11}$)	2 ($4f^{12}$)
Rare earth moment (μ_B)[b]	1.59	2.13	2.12	1.92	1.51
Average Co^{n+} moment (μ_B)	2.31	3.24	2.74	2.44	2.26

[a]From thermogravimetric measurements.

[b]$0.2 \times \mu_{eff}$ ($= g[J(J+1)]^{\frac{1}{2}}$; $g = \frac{3}{2} + [S(S+1) - L(L+1)]/2J(J+1)$).

Table 5
Different spin configurations and effective spin-only moments for octahedrally coordinated Co^{3+} and Co^{4+}

	Unpaired electrons	μ_{eff} (μ_B)[a]
Co^{3+}	$3d^6$	
Low spin	0 ($e_g^0t_{2g}^6$)	0
Intermediate spin	2 ($e_g^1t_{2g}^5$)	2.83
High spin	4 ($e_g^2t_{2g}^4$)	4.90
Co^{4+}	$3d^5$	
Low spin	1 ($e_g^0t_{2g}^5$)	1.73
Intermediate spin	3 ($e_g^1t_{2g}^4$)	3.87
High spin	5 ($e_g^2t_{2g}^3$)	5.92

[a]$\mu_{eff} = 2[S(S+1)]1/2$.

ranging from 2.26 μ_B (for $Tm_{0.20}Sr_{0.80}CoO_{2.73}$) to 3.24 μ_B (for $Dy_{0.20}Sr_{0.80}CoO_{2.71}$). These values are consistent with cobalt moments found for other Sr-doped based cobaltate perovskites with diamagnetic rare earth ions (3.27 μ_B for $Y_{0.20}Sr_{0.80}CoO_3$ [25], 2.87 μ_B for $Y_{0.05}Sr_{0.95}CoO_{2.79}$ [5], 2.92 μ_B for $Ce_{0.10}Sr_{0.90}CoO_{2.80}$ and 3.04 μ_B for $Ce_{0.05}Sr_{0.95}CoO_{2.79}$ [9]). Assigning a unique electronic configuration that accounts for the observed cobalt moments is not a trivial task. Each octahedrally coordinated cobalt ion may be either Co^{3+} or Co^{4+}, and each of those oxidation states may exist in one of three different spin states: low spin (LS), intermediate spin (IS) or high spin (HS). The six different cobalt moments range from 0 μ_B for LS Co^{3+} ($t_{2g}^6e_g^0$—with no unpaired electrons) to 5.92 μ_B for HS Co^{4+} ($t_{2g}^3e_g^2$) (Table 5). A total of nine different possibilities exist, and the combinations of IS Co^{3+}/LS Co^{4+} or IS Co^{3+}/IS Co^{4+} are the ones that gave the closest match to the observed moments. Another issue further complicates this analysis. The high level of oxygen vacancies in these phases means that approximately 10% of the cobalt sites will be five-fold (square pyramidal) coordinate leading to a different distribution of *d*-orbital energies and unpaired electrons.

The susceptibility data for $Gd_{0.20}Sr_{0.80}CoO_{2.72}$ show only two magnetic transitions (T_{c2} at 307 K and T_{c3} at 131 K). Each of the phases (Dy^{3+}–Tm^{3+}) that crystallise with the *Cmma* orthorhombic superstructure show a clear correlation with magnetic behaviour, having an additional sharp magnetic transition (T_{c1}) in the DC susceptibility at ~340 K (Table 4). Preliminary variable temperature neutron powder diffraction studies of $Ho_{0.20}Sr_{0.80}CoO_{2.75}$ and $Tm_{0.20}Sr_{0.80}CoO_{2.73}$ suggest that T_{c1} is associated with an antiferromagnetic phase transition [43]. To date, however, we have not accumulated adequate quality neutron powder diffraction data (with high-resolution and long d-spacings) to allow the full nature of this magnetic structure to be determined. It is our intention to fully characterise the magnetic structure associated with the T_{c1} transition as part of a future study.

Each of the orthorhombic $Ln_{0.20}Sr_{0.80}CoO_{3-\delta}$ phases also show the same two features as observed for $Gd_{0.20}Sr_{0.80}CoO_{2.72}$; an antiferromagnetic transition (T_{c2}) near room temperature and a broad transition (T_{c3}) near 100 K associated with short-range magnetic order.

For comparison with the orthorhombic $Ln_{0.20}Sr_{0.80}CoO_{3-\delta}$ phases, susceptibility data are also presented for $Ho_{0.3}Sr_{0.7}CoO_{3-\delta}$ and $Ho_{0.1}Sr_{0.9}CoO_{3-\delta}$ (Fig. 11(b)); the former shows a T_{c2} transition at ~297 K, while the latter shows a distinct T_{c3} transition at ~92 K. The T_{c2} transitions have previously been shown to be associated with G-type antiferromagnetism in $Ln_{1-x}Sr_xCoO_{3-\delta}$ perovskites ($x\sim 0.7$) [9,16–18], and the T_{c3} transition associated with short-range magnetic cluster-glass formation [5,16–17,26]. Neither $Ho_{0.3}Sr_{0.7}CoO_{3-\delta}$ nor $Ho_{0.1}Sr_{0.9}CoO_{3-\delta}$ show the additional sharp antiferromagnetic transition at temperatures above 330 K associated with the orthorhombic phases $Ln_{0.20}Sr_{0.80}CoO_{3-\delta}$ ($Ln = Dy^{3+}$-Tm^{3+}).

There has already been significant discussion in the literature about the nature of the magnetic transitions T_{c2} and T_{c3}. Using variable temperature powder neutron diffraction, Goossens and co-workers [16,17] have shown (for $Y_{0.33}Sr_{0.67}CoO_{3-\delta}$ and $Ho_{0.33}Sr_{0.67}CoO_{3-\delta}$) that T_{c2} corresponds to long-range G-type antiferromagnetic order with the cobalt moments (of $2\,\mu_B$) aligned parallel to the crystallographic c-axis of the tetragonal cell. Maignan et al. [18] subsequently showed the critical role that oxygen content plays in these materials. In their study of $Y_{0.33}Sr_{0.67}CoO_{3-\delta}$, the as-prepared compound, having a relatively high level of oxygen vacancies ($\delta\sim 0.34$) was found to be an insulating antiferromagnet (with a clear T_{c2} transition). Following further annealing in an 100 atm oxygen atmosphere (600 °C for 12 h) a small increase in oxygen content was observed ($\delta\sim 0.30$) and the compound was found to exhibit metallic ferromagnetism (with the extinction of the T_{c2} transition and an enhancement of the T_{c3} transition). Essentially the same behaviour giving rise only to a T_{c3} transition was observed for the highly doped phases $Ln_{0.05}Sr_{0.95}CoO_{3-\delta}$ ($Ln = Y^{3+}$, Sm^{3+}-Yb^{3+}) [5], where it was shown that different rare earth ions (occupying only 5% of the A-sites) led to a substantial variation in the intensity of the magnetic response.

4. Conclusions

We have shown that a new average orthorhombic superstructure (*Cmma*; $2\sqrt{2}a_p \times 4a_p \times 2\sqrt{2}a_p$) exists for a small family of Sr-doped rare earth perovskite cobaltates $Ln_{1-x}Sr_xCoO_{3-\delta}$ ($Ln = Y^{3+}$, Dy^{3+}, Ho^{3+}, Er^{3+}, Tm^{3+} and Yb^{3+}; $0.75 \leqslant x \leqslant 0.875$). ED reveals an additional weak structural modulation (giving a C-centred $2\sqrt{2}a_p \times 4a_p \times 4\sqrt{2}a_p$ superstructure) that is not apparent in the synchrotron X-ray or neutron powder diffraction data. For larger rare earth ions and either side of the above phase field, the previously reported tetragonal superstructure (*I*4/*mmm*; $2a_p \times 2a_p \times 4a_p$) is present. The average orthorhombic *Cmma* superstructure is the result of a combination of A-site cation and oxygen vacancy ordering. DC magnetic susceptibility measurements show that these orthorhombic phases are associated with an additional magnetic transition at temperatures above ~330 K.

Acknowledgments

The authors acknowledge the allocation of facilities at the European Synchrotron Radiation Facility (experiment numbers: HE1716, HE1849 and HS2970); as well as funding support from the Access to Major Research Facilities Program (proposal number: 04/05-S-07).

References

[1] R.L. Withers, M. James, D.J. Goossens, J. Solid State Chem. 174 (2003) 198.
[2] S. Ya Istomin, J. Grins, G. Svensson, O.A. Drozhzhin, V.L. Kozhevnikov, E.V. Antipov, J.P. Attfield, Chem. Mater. 15 (2003) 4012.
[3] M. James, D. Cassidy, D.J. Goossens, R.L. Withers, J. Solid State Chem. 177 (2004) 1886.
[4] S.Ya. Istomin, O.A. Drozhzhin, G. Svensson, E.V. Antipov, Solid State Sci 6 (2004) 539.
[5] M. James, D. Cassidy, K.F. Wilson, J. Horvat, R.L. Withers, Solid State Sci 6 (2004) 655.
[6] R.H.E. van Doorn, A.J. Burggraaf, Solid State Ionics 128 (2000) 65.
[7] M. James, T. Tedesco, D.J. Cassidy, R.L. Withers, Mat. Res. Bull. 40 (2005) 990.
[8] N.E. Trofimenko, J. Paulsen, H. Ullmann, R. Müller, Solid State Ionics 100 (1997) 183.
[9] M. James, K.S. Wallwork, R.L. Withers, D.J. Goossens, K.F. Wilson, J. Horvat, X.L. Wang, M. Colella, Mater Res. Bull. 40 (2005) 1415.
[10] S. Hébert, A. Maignan, V. Caignaert, V. Pralong, D. Pelloquin, B. Raveau, Solid State Commun 134 (2005) 815.
[11] S.J. Skinner, Int. J. Inorg. Mater 3 (2001) 113.
[12] H.Y. Tu, Y. Takeda, N. Imanishi, O. Yamamoto, Solid State Ionics 100 (1997) 283.
[13] S.B. Adler, Solid State Ionics 111 (1998) 125.
[14] A.V. Kovalevsky, V.V. Kharton, V.N. Tikhonovich, E.N. Naumovich, A.A. Tonoyan, O.P. Reut, L.S. Boginsky, Mater. Sci. Eng. B 52 (1998) 105.
[15] V.V. Kharton, A.A. Yaremchenko, A.V. Kovalevsky, A.P. Viskup, E.N. Naumovich, P.F. Kerko, J. Membr. Sci. 163 (1999) 307.
[16] D.J. Goossens, K.F. Wilson, M. James, J. Phys. Chem. Solids 66 (2005) 169.
[17] D.J. Goossens, K.F. Wilson, M. James, A.J. Studer, X.L. Wang, Phys. Rev. B 69 (2004) 134411.
[18] A. Maignan, B. Raveau, S. Hélbert, V. Pralong, V. Caignaert, D. Pelloquin, J. Phys. Condens. Matter 18 (2006) 4305.
[19] V.V. Sikolenko, E.V. Pomjakushina, S.Ya. Istomin, J. Magn. Magn. Mater 258 (2003) 300.
[20] G. Briceno, H. Chang, X. Sun, P.G. Schultz, X.D. Xiang, Science 270 (1995) 273.
[21] R. Mahendiran, A.K. Raychaudhuri, Phys. Rev. B 54 (1996) 16044.
[22] S. Yamaguchi, H. Taniguchi, H. Takagi, T. Arima, Y. Tokura, J. Phys. Soc. Japan 64 (1996) 1885.
[23] M.A. Senaris-Rodriguez, M.P. Breijo, S. Castro, C. Rey, M. Sanchez, R.D. Sanchez, J. Mira, A. Fondado, J. Rivas, Int. J. Inorg. Mater 1 (1999) 281.
[24] A. Maignan, S. Hebert, V. Caignaert, V. Pralong, D. Pelloquin, J. Solid State Chem. 178 (2005) 868.
[25] S. Balamurugan, E. Takayama-Muromachi, J. Solid State Chem. 179 (2006) 2231.

[26] R. Ang, Y.P. Sun, X.B. Zhu, W.H. Song, X.G. Luo, X.H. Chen, Solid State Commun 138 (2006) 255.
[27] K.H. Ryu, K.S. Roh, S.J. Lee, C.H. Yo, J. Solid State Chem. 105 (1993) 550.
[28] J.W. Kang, K.H. Ryu, C.H. Yo, Bull. Korean Chem. Soc. 17 (1995) 600.
[29] S.K. Jeong, M.G. Kim, K.H. Kim, C.H. Yo, Bull. Korean Chem. Soc. 17 (1996) 794.
[30] P.V. Vanitha, A. Arulraj, P.N. Santhosh, C.N.R. Rao, Chem. Mater. 12 (2000) 1666.
[31] K. Yoshii, H. Abe, A. Nakamura, Mater Res. Bull. 36 (2001) 1477.
[32] H.W. Brinks, H. Fjellvag, A. Kjekshus, B.C. Hauback, J. Solid State Chem 147 (1999) 464.
[33] M. Paraskevopoulos, J. Hemberger A. Krimmel, A. Loidl, Phys. Rev. B 63 (2001) 224416.
[34] A. Krimmel, M. Reehuis, M. Paraskevopoulos, J. Hemberger, A. Loidl, Phys. Rev. B 64 (2001) 224404.
[35] Y. Takeda, H. Ueno, N. Imanishi, O. Yamamoto, N. Sammes, M.B. Philipps, Solid State Ionics 86 (1996) 1187.
[36] V.G. Sathe, A.V. Pimpale, V. Siruguri, S.K. Paranjpe, J. Phys.: Condens Matter 8 (1996) 3889.
[37] A. Mineshige, M. Inaba, T. Yao, Z. Ogumi, K. Kikuchi, M. Kawase, J. Solid State Chem. 121 (1996) 423.
[38] J. Kirchnerova, D.B. Hibbert, J. Mater. Sci. 28 (1993) 5800.
[39] T. Motoohashi, V. Caignaert, V. Pralong, M. Hervieu, A. Maignan, B. Raveau, Phys. Rev. B 71 (2005) 214424.
[40] A. Maignan, D. Pelloquin, D. Flahaut, V. Caignaert, J. Solid State Chem. 177 (2004) 3693.
[41] M.C. Viola, M.J. Martinez-Lope, J.A. Alonso, J.L. Martinez, J.M. de Paoli, S. Pagola, J.C. Pedregosa, M.T. Fernandez-Diaz, R.E. Carbonio, Chem. Mater. 15 (2003) 1655.
[42] M. James, A. Tedesco, D. Cassidy, M. Colella, P.J. Smythe, J. Alloys Comp 419 (2006) 201.
[43] Unpublished data.